Materials and Design 198 (2021) 109324

Contents lists available at ScienceDirect

Materials and Design

journal homepage: www.elsevier.com/locate/matdes

Inkjet-printing-derived lead-zirconate-titanate-based thick films for printed electronics

Danjela Kuscer [a,*], Silvo Drnovšek [a], Franck Levassort [b]

[a] Jožef Stefan Institute, Jamova cesta 39, SI-1000 Ljubljana, Slovenia
[b] GREMAN UMR7347, University of Tours, CNRS, INSA CVL, Tours, France

HIGHLIGHTS

- Predesigned PZTNb films were obtained by piezoelectric inkjet printing using aqueous suspension of nano-sized powders.
- Liquid phase PbO leads to sintering of nano PZTNb with moderate densification rate in broad temperature range of 450 °C.
- PbO contributes to stress relaxation, lowering processing temperature to 850 oC and formation of defect-free PZTNb films.
- Inkjet-printed film with single-phase structure exhibited thickness coupling factor of 46 %, comparable to bulk ceramics.

GRAPHICAL ABSTRACT

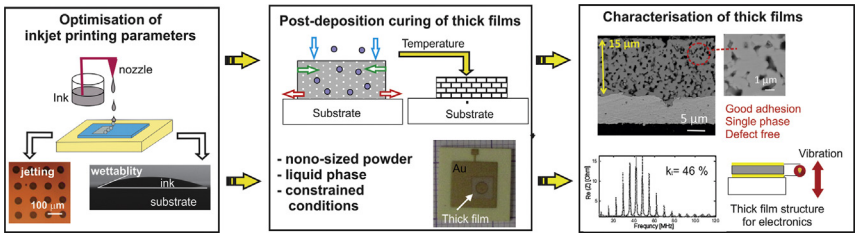

ARTICLE INFO

Article history:
Received 7 August 2020
Received in revised form 10 November 2020
Accepted 10 November 2020
Available online 12 November 2020

Keywords:
Inkjet printing
Thick films
Piezoelectricity
Lead zirconate titanate
Electromechanical properties
Printed electronic

ABSTRACT

We have investigated the processing of lead-zirconate-titanate-based thick films by inkjet printing Pb$(Zr_{0.53}Ti_{0.47})_{0.98}Nb_{0.02}O_3$ with a 6 mol% excess of PbO nanosized powder dispersed in water. Different waveforms were employed to determine the optimum size and shape of the drops. A uniform, defect-free pattern with dimensions of 4 mm × 4 mm can be printed using 20 V and a drop spacing of 20 µm. The inkjet-printed films were heated to 400 °C to remove the organics and subsequently sintered at 750 and 850 °C. The correlations between the density, grain size and electromechanical properties of the thick films and bulk ceramics are qualitatively discussed. A thickness coupling factor of 46% was obtained for a 15-µm-thick film sintered at low temperature of 850 °C, which is comparable to the value of the bulk ceramic with an identical nominal chemical composition. Our results are important for the economic and environmental-benign printing of piezoelectric materials applicable in variety of electronic devices, such as sensors, actuators, transformers, piezoelectric energy harvesters and transducers.

1. Introduction

Piezoelectric materials can convert electrical energy into mechanical energy, or vice versa, a characteristic that is exploited in a variety of devices, such as sensors, actuators, transformers, piezoelectric energy harvesters and transducers. Miniature devices frequently utilise

* Corresponding author.
E-mail address: danjela.kuscer@ijs.si (D. Kuscer).

https://doi.org/10.1016/j.matdes.2020.109324

piezoelectrics that are based on lead zirconate titanate, with a composition close to the morphotropic phase boundary, $PbZr_{0.52}Ti_{0.48}O_3$ (PZT), in the form of thick film. To provide an effective and stable response from the device, the piezoelectric material should have a proper geometry and a proper set of material constants, such as a high piezoelectric strain and voltage constant, high electromechanical coupling factors, a high mechanical quality factor and an appropriate acoustic impedance [1–5]. Thus, the piezoelectric thick film must be of high quality, i.e., it should be chemically homogeneous without any secondary phases, should have the preferred crystal structure and a microstructure with the required homogeneity, density and grain size, should be well adhered to, and should not chemically interact with, the substrate [6].

To date, screen printing is the most often used technique in the electronics industry for the processing of patterned thick-film structures. It requires the suspension of particles that are squeezed through a mask onto a substrate, and subsequently sintered at elevated temperature, typically above 900 °C [7]. Piezoelectric inkjet printing (PIJ) has been proposed as an alternative method. Unlike screen printing, PIJ does not require a mask, but the pattern is designed digitally and sent to the printer. The printer is able to deposit a drop of a suspension of nanoparticles, i.e., ink, on to an arbitrary surface of the substrate by applying a pressure pulse through the nozzles, typically 20–50 μm in diameter, to form a predefined pattern with a reliable lateral resolution of μm. Next, the layer needs to be sintered to develop the microstructure, mechanical strength and suitable functional properties. Inkjet printing technology provides possibilities for short production runs and customization because of the computer-controlled, mask-less deposition of various materials on many substrates, economic and sustainable production due to a low energy consumption and small amounts of waste in production, a quick response time and scalability. The limitations include costly print heads, which are prone to clogging, short life span of the inks and limited availability of the complex-composition inks [8,9].

A lot of research on inkjet printing is related to the development of ink made from metal-oxide nanoparticles and proving its jettability, but the post-deposition curing is typically not addressed [10]. The investigations on post-deposition curing have been carried out mostly for metal nanoparticles, such as silver [11] or for simple metal oxides such as NiO [12], highlighting the capability of using them as an electrode. There have been some efforts to process piezoelectric, complex-composition, metal-oxide thick films. So far, a $BaTiO_3$–epoxy resin composite layer was processed by inkjet printing and annealing at 250 °C. The results were promising, demonstrating effective energy harvesting [13]. But pure $BaTiO_3$ has a higher potential to harvest energy than a composite since the electromechanical response of pure $BaTiO_3$ is expected to be larger than that of the composite. Lead-zirconate titanate thick films were processed by inkjet printing following by laser sintering. The authors reported on the formation of defects, which prevents the functional characterization of the thick film [14].

In our previous work [15–17] we prepared an aqueous suspension of lead zirconate titanate nano-sized powder that satisfies the requirements for a Dimatix piezoelectric inkjet printer with a nozzle size of 21 μm [18], i.e., a stable suspension with the particle size d_{v100} below 500 nm, a viscosity of ~10 mPas, a surface tension ~30 mN/m and moderate drying at room temperature. A few-micrometre-sized powder was comminuted to the sub-micrometre range and simultaneously or subsequently electrosterically stabilised in aqueous alkaline media with polyacrylic acid or polyethilene imine. The surface tension of the suspension was adjusted by non-ionic amphiphilic phenyl ethoxylate, and the viscosity and drying by the addition of glycerol. The optimisation of the inkjet printing process in terms of the waveform resulted in the high positional accuracy of the drops on the rough Au-covered alumina substrate with a root-mean-square $R_q = 1.92$ and drops with uniform size of ~40 μm after drying at 400 °C both reflecting in a high lateral resolution of a few micrometres.

With the aim to process single-phase, dense piezoelectric thick films, we sintered them at elevated temperatures. The preliminary sintering experiments of lead-zirconate-titanate thick films with a few-tens-of-nm-sized particles revealed that at 1100 °C we obtained locally, very dense regions separated with micrometre-sized defects, which enabled only local functional characterization of the thick film [17], while after heating at 850 °C the thick films were relatively porous [16]. The formation of defects and/or the porous structure of the thick films are attributed to the rapid densification of the nano-sized powder constrained in the rigid substrate and/or insufficient relaxation of the stresses [19].

The nanometre-sized particles are absolutely necessary for jetting the particles through ~20-μm-sized nozzles, which enables the processing of thick-film structures with a micrometre-sized lateral resolution and a line width of ~50 μm [16]. However, the densification rate for PZT-based ceramic is inversely proportional to the cube of the grain size [20], meaning that the densification rate for a nano-sized powder is very high. Consequently, the stresses cannot relax in such a timescale and thus the defects are formed in the thick film deposited on a rigid substrate. A possible solution to prevent the formation of defects is to lower the processing temperature and thus lower the densification rate and/or to promote the stress relaxation during the densification of the thick films. It was shown that the addition of excess PbO to the lead-based perovskites enables sintering in the presence of a liquid phase, which decreased the onset-on sintering temperature and resulted in denser thick films compared to their stoichiometric counterparts. When the excess PbO is successfully eliminated from the thick films during sintering, the dielectric and piezoelectric properties of the thick films are significantly improved [6].

This motivated us to focus the current investigation on improving the density and preventing the formation of defects in inkjet-printed, nanosized, lead-zirconate-titanate-based thick films. Earlier investigations have been conducted on $Pb(Zr_{0.53}Ti_{0.47})_{0.98}Nb_{0.02}O_3$ (PN). In this report we explore the effect of adding PbO on the jetting, post-deposition curing, development of microstructure and electromechanical characterization of thick films, namely $Pb(Zr_{0.53}Ti_{0.47})_{0.98}Nb_{0.02}O_3$ with 6 mol% excess of PbO (PN6). This study highlights the capability of PbO to lower the processing temperature and slow the densification rate of nanoparticles, which enable stress relaxation and prevent the formation of defects in the piezoelectric thick-film structure. The study demonstrates the high potential of inkjet printing technology and subsequent sintering for the economic processing of high-quality, complex-composition piezoelectric thick films applicable in electronic devices.

2. Experimental

Powder of $Pb(Zr_{0.53}Ti_{0.47})_{0.98}Nb_{0.02}O_3$ with 6 mol% excess of PbO (denoted PN6) was synthesised from PbO (99.9%, Aldrich), ZrO_2 (99.1%, Tosoh), TiO_2 (99.8%, Alfa Aesar) and Nb_2O_5 (99.9%, Sigma Aldrich) by solid-state synthesis at 1100 °C. The as-synthesised powder (μ-PN6) was milled for 3 h in ultrapure water in a colloidal mill (MiniCer, Netzsch, Selb, Germany) and afterwards dried at 105 °C. The powder is denoted as n-PN6. The details of the synthesis of the powder without any excess of PbO, i.e., $Pb(Zr_{0.53}Ti_{0.47})_{0.98}Nb_{0.02}O_3$ (PN), and the milling procedure are given elsewhere [15,16].

Some 10 vol% of n-PN6 powder was stabilised in ultrapure water with 6 wt% of polyethyleneimine (PEI, molecular weight ~ 10,000, Alfa Aesar, Karlsruhe, Germany) with respect to the solids load. The suspension with a pH of 8 was homogenised in a planetary ball mill (PM 400, Retsch, Haan, Germany) for 2 h and subsequently sonicated for 10 min with an energy of 800 kJ and an amplitude of 40% in an ice bath using a Vibra cell VC 33 (Sonics & Materials, Newtown, USA). The suspension for inkjet printing, n-PN6 ink, additionally contained 20 vol% of glycerol and 0.1 vol% of phenyl ethoxylate.

The ink was jetted onto the corundum substrates (Kyocera A493, 99.6%, Neuss, Germany) covered with a gold electrode (Au/AO).

The electrode was prepared by the screen printing of the gold paste (ELS 8884-G, ElectroScience, King of Prussia, PA, USA) onto the corundum and firing at 900 °C for 10 min.

The ink was jetted through a nozzle size of 21 μm using a dischargeable cartridge (DMC-11610, Fuji Film, Santa Clara, CA, USA) and a piezoelectric inkjet printer (Dimatix 2831, Fuji Film, Santa Clara, CA, USA). To optimize the jetting conditions, we printed the drops with a drop spacing (DS) of 100 μm onto a Si/SiO_2 substrate (University Wafer) at 20, 25 and 30 V using the shape of the waveform (WF) reported in [16]. We varied the total time and the duration of the corresponding segments (Table 1). Under optimal jetting conditions, we printed the square-shaped pattern with dimensions of 4 mm × 4 mm onto Au/AO at room temperature, using a DS of 20 μm.

The samples consisted of three layers of PN6 on Au/AO inkjet printed under identical conditions. The first layer was dried at 50 °C for 10 min and consequently annealed at 400 °C for 1 h in air in a tube furnace with heating and cooling rates of 1 °C/min. A second layer was dried at 50 °C for 10 min. The third layer was annealed at 400 °C for 1 h and then sintered at 750 and 850 °C for 2 h in air in the presence of $PbO/PbZrO_3$ packing powder. The samples sintered at 750 and 850 °C are denoted P750 and P850, respectively.

The dynamic sintering curves of the PN and PN6 powder compacts were recorded upon heating with a rate of 5 K min^{-1} to 1300 °C in an air atmosphere using an optical dilatometer (Leitz V. 1A, Leitz, Wetzlar, Germany). The powders were pressed in a steel mould with a diameter of 6 mm and using a uniaxial pressure of 100 MPa. The dimensions of the powder compacts were continuously measured from digitalized images and the relative shrinkages (Δl/l) were determined.

The particle size and the particle-size distribution of the particles were determined with a static light-scattering particle size analyser (Microtrac S3500, Montgomeryville, PA, USA). The results were derived from the volume particle size distribution (d_v).

The zeta-potential (ZP) of the particles was measured in a KNO_3 solution at pH 8 using a zeta-potential analyser (Zeta PALS, Brookhaven, Holtsville, NY, USA). The pH of the diluted suspensions was adjusted with NaOH (0.1 M, Alfa Aesar, Karlsruhe, Germany).

The viscosities of the suspensions were measured at 25 °C using shear rates in the range 1–100 s^{-1} with a CC 27 cylindrical system and a rheometer (Physica MCR 301, Anton Paar, Graz, Austria). The surface tension and the contact angle of the suspensions on the Si and Au/AO substrates were measured at 25 °C with an optical tensiometer (EasyDrop DSA20E, Kruss GmbH, Hamburg, Germany)

Thermogravimetric (TG) and differential thermal analyses (DTA) were performed simultaneously using a Netzsch STA 409 analyser (Hann, Germany). The evolved gases were monitored with a mass spectrometer (Balzers Thermostar GSD 300 T). The analyses were performed in PtRh crucibles. The samples were heated from 25 °C to 650 °C with a heating rate of 2 K min^{-1} in a flow of synthetic air. The suspension was dried prior to the analyses at 50 °C for 1 h.

The X-ray powder diffraction (XRD) data of the samples were collected at room temperature with a PANalytical X'Pert PRO high-resolution diffractometer using Cu-$K_{\alpha 1}$ radiation (l = 1.5406 Å) in the reflection geometry. The data were collected in the 2θ range from 20 to 70° with a step of 0.017° and a total integration time of 200 s per. The phases present in the samples were identified using the PDF-4 database (release 2019). The lattice parameters of the phases were obtained with a Rietveld refinement using the Topas R (Bruker AXS, Karlsruhe, Germany) software package. A fundamental parameters approach was used for the peak-shape fitting. The zero-error shift, the scale factor, the unit-cell size, and one profile parameter (the crystallite size) were refined for each phase to minimize the difference between the experimental and calculated patterns.

The powder morphology, top surfaces and polished cross-sections of the sintered thick films were investigated using a scanning electron microscope (SEM; JSM–7600F, Tokyo, Japan). The relative density of the thick films was evaluated from binary images of the original SEM cross-section images using ImageJ software (National Institute of Health, USA).

For the electrical characterization, top gold electrodes with a diameter of 2 mm were sputtered on the sintered samples (5 Pascal, Italy). The capacitance and loss factor (tan δ) were measured on non-poled samples at 1 kHz with an HP 4192A LF Impedance Analyser.

The P850 thick films were poled at 4 kV/mm for 40 min at 120 °C in an oil bath. The electromechanical properties of the thick films in thickness mode were deduced from a measurement of the complex electrical impedance as a function of the frequency around the fundamental thickness-mode resonance using a HP4395 spectrum analyser (Agilent Technologies Inc., USA). For that, the theoretical electrical impedance was also computed using the KLM equivalent electrical circuit [21]. This one-dimensional model considers the three inert layers in the structure (alumina substrate and the two electrodes). The data of these three layers must be accurately known to deduce, with a fitting process on the experimental impedance, several thick-film parameters such as the effective-thickness-mode coupling factor k_t, the dielectric permittivity at constant strain (ε_{33}^S), the mechanical losses δ_m and the longitudinal wave velocity (V_L) related to the elastic constant at a constant electrical displacement (C_{33}^D) [3].

Table 1
The waveforms for printing n-PN6 ink. The voltage and the duration of segments are denoted as V and t. Total duration of the waveform is denoted as t_{total}.

Waveform	t_{total} [μs]	Segment A		Segment B		Segment C		Segment D	
		V_A [V]	t_A [μs]	V_B [V]	t_B [μs]	V_C [V]	t_C [μs]	V_D [V]	t_D [μs]
WF 8-20	8.00	0	2.16	20	2.88	5.4	1.75	0	1.21
WF 8–25	8.00	0	2.16	25	2.88	6.75	1.75	0	1.21
WF 8–30	8.00	0	2.16	30	2.88	8.1	1.75	0	1.21
WF 14–20	14.00	0	3.78	20	5.04	5.4	3.06	0	2.12

3. Results and discussion

3.1. Properties of the PN and PN6 powders

After the colloidal milling the PN6 consisted of nano-sized particles ranging from a few tens of nm to ~400 nm (Fig. 1a). The broad particle size distribution with two maxima at ~200 nm and ~ 400 nm (Fig. 1b) and sizes up to 9.2 μm (d_{v100}) indicated that the particles were agglomerated. Colloidal milled powder without an excess of PbO, i.e., PN, had a similar particle size [16], while the particle size of the as-synthesised powders was much larger, in the micrometre-range [15].

The dynamic shrinkage-temperature curves of PN and PN6 are significantly different (Fig. 2): the onset-on-sintering temperature for PN6 is lower than that of the PN, regardless of the particle size, i.e., 700 °C and 1000 °C, respectively. The lowering of the onset-on-sintering temperature for lead-based perovskites with an excess of PbO is a well-known phenomenon [22,23]. It is attributed to the low melting temperature of PbO, i.e., 888 °C. Upon heating the PbO melts, forming a PbO-rich liquid phase, which promotes the densification during the initial and intermediate stages of sintering.

Comparing the shrinkage-temperature curves for the as-synthesised and colloidal milled PN6, we can see that both powders started to shrink already at 700 °C. The as-synthesised powder (μ-PN6) reached a shrinkage of 17% at 1180 °C and the colloidal milled powder (n-PN6) 19% at 1160 °C. The powders densified over a broad and similar temperature range but the shrinkage of the n-PN6 was larger than that of the μ-PN6 at temperatures higher than 700 °C. The colloidal milled powder, n-PN, exhibited the most rapid shrinkage rate: it shrank between 1000 and 1120 °C, and by 22% at 1120 °C. The as-synthesised powder, μ-PN, shrank between 1000 and 1300 °C and reached a shrinkage of

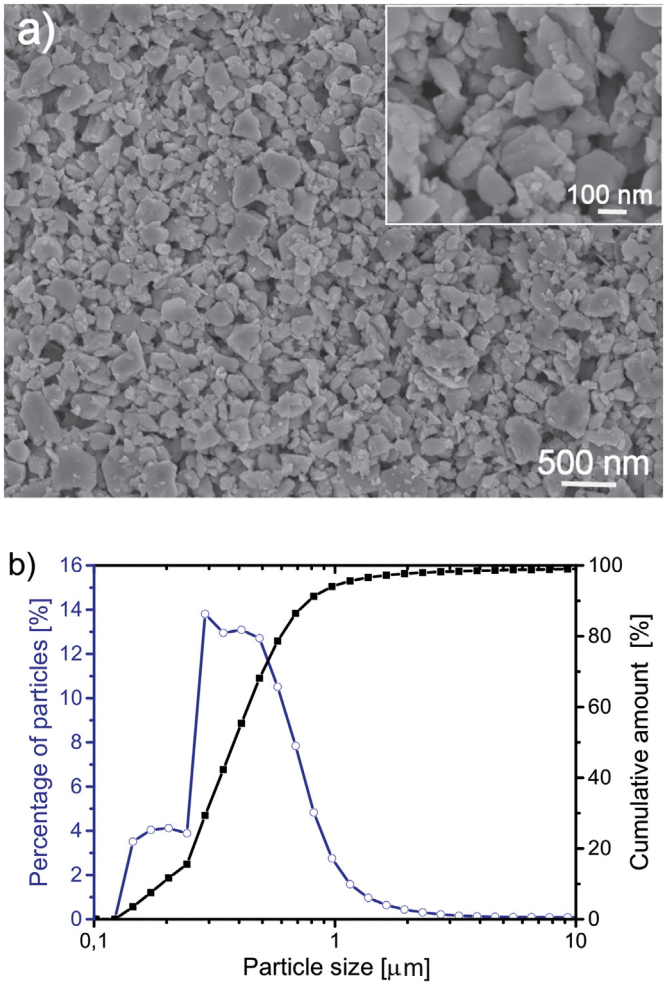

Fig. 1. Colloidal milled n-PN6 powder a) SEM image b) particle size distribution (o) and cumulative amount of the particles (■) determined by laser diffraction.

20% at 1300 °C. Similar to the PbO-excess powders, the shrinkage of n-PN was larger than the that of μ-PN (Fig. 2b). However, the PN powders shrank in a narrower temperature range than the PN6 powders, regardless of the particle size. These results are entirely expected and confirm that powder characteristics such as particle size and chemistry are essential factors controlling the densification kinetics.

The exceptionally rapid densification rate of the n-PN could lead to large misfit stresses in the thick-film structure. This could result in the formation of defects similar to those reported in [17] for the colloidal milled PZT inkjet printed on an alumina substrate after sintering at 1100 °C. We assume that in the thick-film structure composed of μ-PN6, which densifies over a broader temperature range and in the presence of the liquid phase, the misfit stresses will relax in such a way that they do not results in macroscopic defects in the thick-film structure.

3.2. Inkjet printing

The n-PN6 powder was stabilised in water with polyethylene imine and deagglomerated by sonication the suspension for 10 min. The glycerol was added to the suspension to increase its viscosity and decrease its drying rate, and the phenyl ethoxylate to decrease its surface tension to values suitable for inkjet printing. The details are described elsewhere [16]. The resulting ink consisted of well-dispersed particles with a normal particle size distribution, a d_{v50} of 280 nm and a d_{v100} of 810 nm. The zeta-potential of +55 ± 3 mV implied long-term stability of the suspension. The ink had a viscosity of 10 mPas at a shear rate of 100 s^{-1} and a surface tension of 30 mN/m, which matches exactly the requirements of the selected inkjet printer. The contact angle of the ink on the silicon and Au/AO substrates was similar, 25 and 20 degrees, respectively. The inverse Ohnesorge number (Z) of 3.5 is in the experimentally determined printable range for aqueous metal-oxide-based suspensions [8,9].

In addition to the properties of the ink, the shape of the waveform, its duration and the applied voltage are the most widely recognized factors controlling the resolution of the printing structure and must be optimised case-by-case [8].

The jettability of the ink at 20, 25 and 30 V and the constant duration of the waveform of 8 ms, i.e., WF 8–20, WF 8–25 and WF 8–30, revealed that the drop size decreases and the position accuracy increases with the decreasing voltage (Fig. 3 a–c, Table 2). At 30 V the drops were spherical with diameters of 65 μm and formed a repeatable pattern with a drop spacing of 103 μm and a positional accuracy of 8.3 μm. The small drops next to the main drop indicate the formation of satellites. Low position accuracy and satellite formation characterised for WF 8–30, are detrimental for processing high-resolution structures. From the shape of the drops jetted at 25 V we can see that satellites landed at the edge of the main drop, which slightly distorted the spherical shape of the drops. The drops were ordered at a drop distance of 101 μm with a positional accuracy of 2.4 μm. A decrease a voltage to 20 V further improved the characteristics of the pattern. The 50-μm-

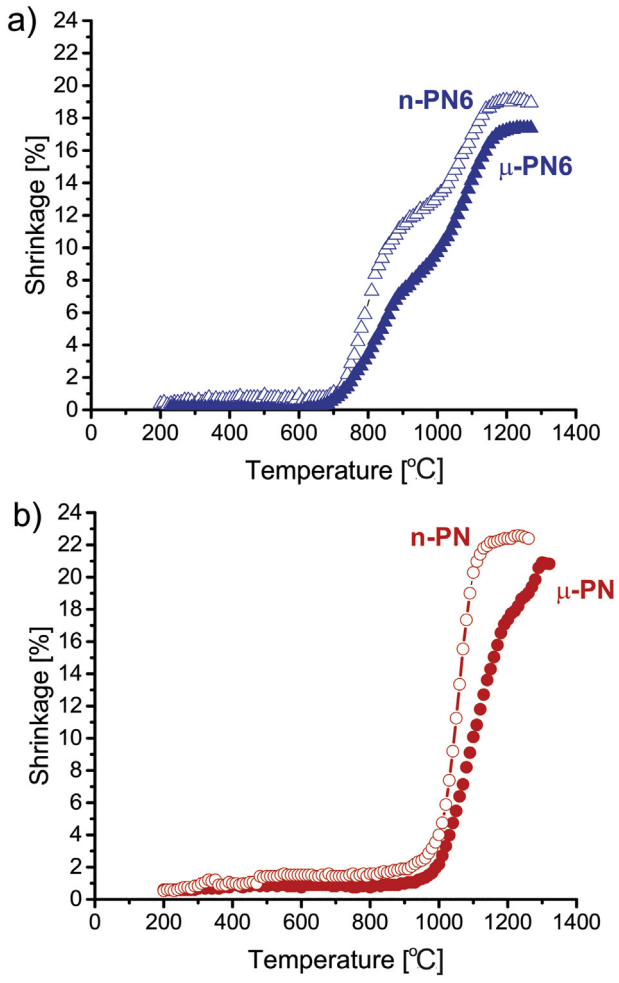

Fig. 2. Dynamic shrinkage – temperature curves for as-synthesised (μ) and colloidal-milled (n) powders. a) PN6 and b) PN.

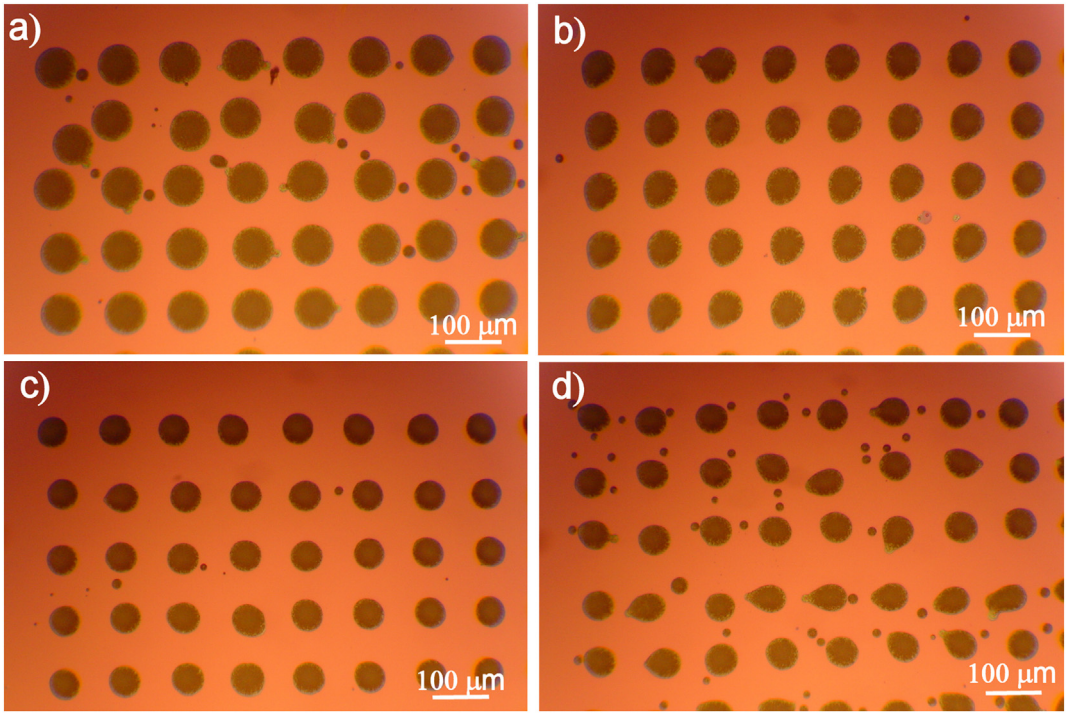

Fig. 3. Drops of n-PN6 in. jetted onto the Si/SiO_2 at (a) WF 8–30, (b) WF 8–25, (c) WF 8–20 and d) WF 14–20.

Table 2
Drop diameter, drop distance and quality-grade evaluation of n-PN6 in. on silicon substrate jetted at various waveforms.

Waveform	Diameter [µm]	Drop spacing [µm]	Quality grade
WF 8–30	65 ± 1.0	103 ± 8.3	need improvement
WF 8–25	54 ± 1.2	101 ± 2.4	good
WF 8–20	50 ± 0.9	100 ± 1.5	excellent
WF14-20	52 ± 1.7	105 ± 11	need improvement

sized spherical drops formed a repeatable pattern with a drop spacing of 100 µm, which is identical to the predefined value and a very high positional accuracy of 1.5 µm. Lowering the voltage from 30 V to 20 V is a promising approach to minimize the formation of satellites, decrease the drop size and increase the position accuracy which all together improve significantly the quality of the pattern.

Prolonging the duration of the waveform from 8 to 14 ms at 20 V (WF 14–20) resulted in a pattern of drops with diameters of 52 µm, which is very similar to the size of the drops jetted at 8 ms. However, we can observe the satellites next to almost every main drop and that the drops are ordered with a relatively low positional accuracy of 11 µm.

Extending the duration of the waveform led to the formation of satellites and reduced positional accuracy which is reflected in inadequate-quality pattern.

After optimizing the jetting conditions, we printed a square-shaped pattern with dimensions of 4 mm × 4 mm onto the Au/AO substrate at 20 V, a waveform duration of 8 ms and a drop spacing of 20 µm. Fig. 4a illustrates that the pattern was uniform with well-defined square shape. The edges were straight and relatively sharp as evident from optical microscopy image on Fig. 4b. The higher-magnification image revealed that the n-PN6 layer were uniform and without any macroscopic defects (Fig. 4c).

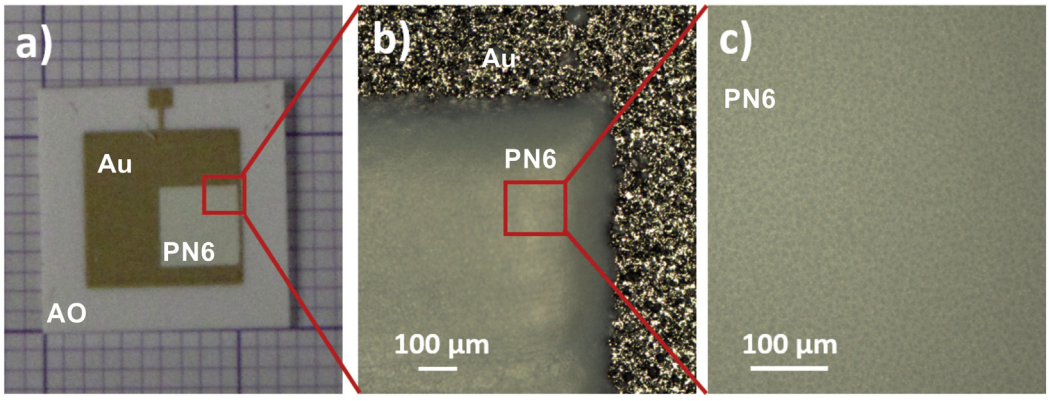

Fig. 4. a) Image of inkjet printed n-PN6 on Au/AO substrate; b) optical microscopy image showing the inkjet printed structure n-PN6 at the edge; c) optical microscopy image showing the inkjet printed structure n-PN6 in its centre.

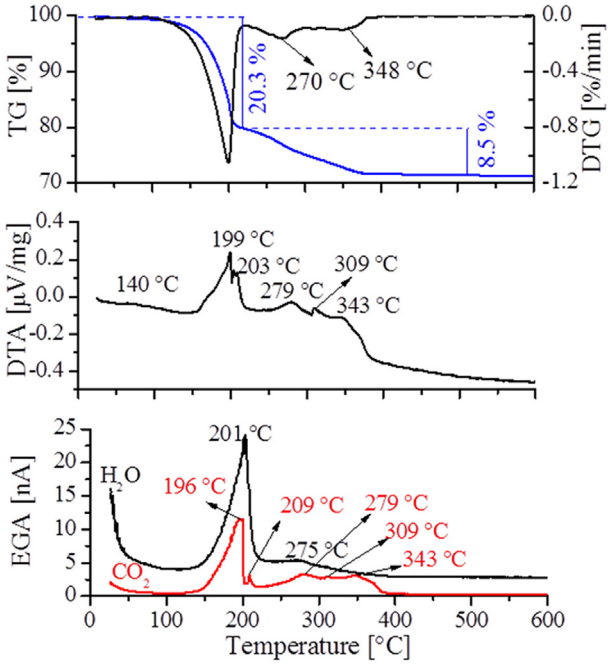

Fig. 5. TG, DTA and EGA curves of the n-PN6 in. dried at 50 °C for 1 h.

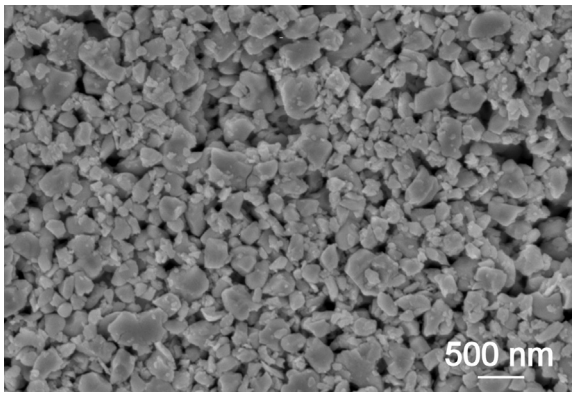

Fig. 6. SEM image of the surface of inkjet printed PN6 pattern annealed at 400 °C.

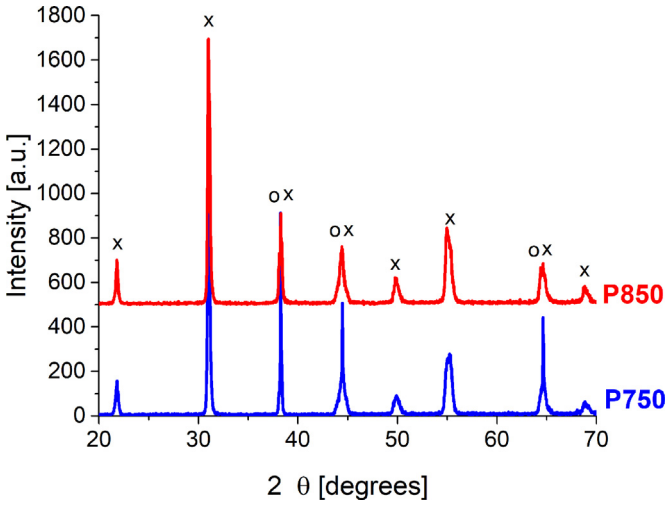

Fig. 7. XRD patterns of P750 and P850. x - perovskite, o - Au.

Table 3
Lattice parameters and amount of tetragonal (T) and rhombohedral (R) phases in P750 and P850. Number in brackets defines the experimental error.

Sample	Amount of phase [%]		Lattice parameters			
	T	R	T		R	
			a [nm]	c [nm]	a [nm]	c [nm]
P750	36(4)	64(6)	0.4046(2)	0.4124(2)	0. 5767(5)	1.4156(1)
P850	40(4)	60(6)	0.4052(1)	0.413(3)	0. 5776(5)	1.418(2)

3.3. Thermal treatment of the ink-jet printed patterns

In order to determine the optimum processing temperature for the printed structures, we performed thermal analyses of the n-PN6 ink. Fig. 5 shows the TG/DTG, DTA and EGA curves. The TG curve revealed a two-step decomposition with a total mass loss of 28.8 wt% upon heating to 600 °C. In the first step, from 25 °C to 220 °C, the major mass loss occurred (20.3%). In the second step, 8.5% of the mass was lost, with complete decomposition up to 400 °C. From the DTA curve a strong exothermic peak was observed with the onset temperature at 140 °C and a maximum at 199 °C accompanied by two EGA peaks, indicating the loss of H_2O and CO_2 from the sample. The evolution of CO_2 was also confirmed by the presence of weak exothermic peaks at 279 °C, 309 °C and 343 °C. The thermal analysis revealed that all the organic additives in the ink decomposed by heating to 400 °C.

The structure of the designed pattern annealed at 400 °C showed a continuous and completely homogeneous layer that consisted of submicrometre-sized particles (Fig. 6). A comparison of the SEM images of the annealed pattern's surface and the milled powder (Fig. 1a) revealed that the powder morphology was very much preserved after the thermal treatment. The particles had similar sizes and shapes and the powder did not densify at 400 °C, which agrees with shrinkage-temperature curve (Fig. 2 a).

3.4. Sintering of thick films at 750 and 850 °C

Based on the dynamic sintering curves of the n-PN6 powder, we sintered the thick films at 750 °C and 850 °C. The former was selected as the point where the powder compact started to shrink and the shrinkage was low, i.e., 2.9%, while the latter was selected as the point of extensive shrinkage, i.e., 9.9%.

After the sintering we did not observe any macroscopic defects on the surface of the thick films and the films were well adhered to the substrate. The XRD patterns of P750 and P850 revealed that the thick films exhibited a perovskite crystal structure as a mixture of tetragonal phase (PDF 01-70-4060) and rhombohedral phase (PDF 04–002-9086) (Fig. 7). The amounts of phases and the lattice parameters of P750 and P850 are similar within the experimental error (Table 3).

The microstructure of the thick films was homogeneous, without any density gradient in either the longitudinal or transversal direction (Fig. 8). The thick film sintered at 750 °C (P750) was 18 μm thick with a relative density of 78%. The sub-micrometre-sized grains were interconnected with necks indicating an initial stage of sintering in agreement with a dynamic shrinkage. See the temperature curve for PN6 (Fig. 8a, Fig. 2a). At 850 °C the thick film was slightly thinner, i.e., 15 μm, but its density increased to 86%. In addition, the larger grains with sizes up to ~2 μm indicated grain growth that is characteristics for the later sintering stages (Fig. 8 b). The P850, derived from nanopowder was able to reach higher density compared to thick films prepared with other technologies from micrometre-sized powders but sintered at higher temperature (screen printing at 900 °C, electrophoretic deposition at 950 °C) [3,24] The densification of the thick films already at 750 °C can be ascribed to the PbO phase. Note that 750 °C is far too

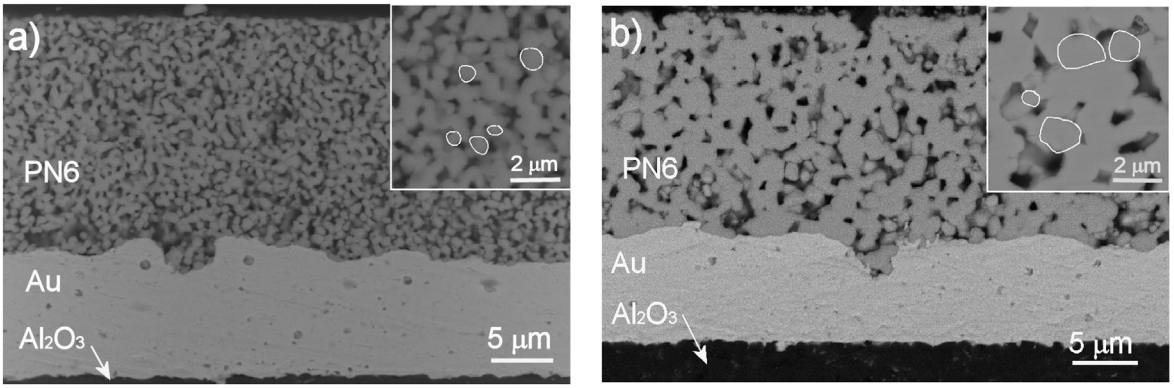

Fig. 8. Cross-section SEM images of the thick films on alumina substrates a) P750 and b) P850. The insets show the PN6. An example of grain is identified by a circle.

low for the densification of the μ-PN and n-PN by solid-state sintering (Fig. 2b). According to the literature, the excess PbO that was deliberately added to the powder, forms a PbO-rich liquid phase at elevated temperatures. This phase segregates at the grain boundaries and promotes the densification of the material [23,25,26]. However, when PbO is present in the sintered material, it deteriorates the functional properties of the piezoelectric material [6].

We did not detect any PbO-rich phase in the sintered layers, despite the very careful examination of the microstructure. Here we take advantage of the high vapour pressure of PbO over the PZT [27], which facilitates the sublimation of PbO from the thick films at the sintering temperatures. The relative density of the P750 and P850 was below 90%, and thus we expect open porosity. The large area of n-PN6 exposed to the atmosphere promotes the sublimation of PbO from the films during processing. Evidently, in our case the sintering time of 2 h was long enough for 6 mol% of excess PbO and enabled densification of the n-PN6 thick films in the initial stage of sintering, but sublimated from the thick films in the later stage of sintering, thus resulting in single-phase PN6 thick films without any PbO.

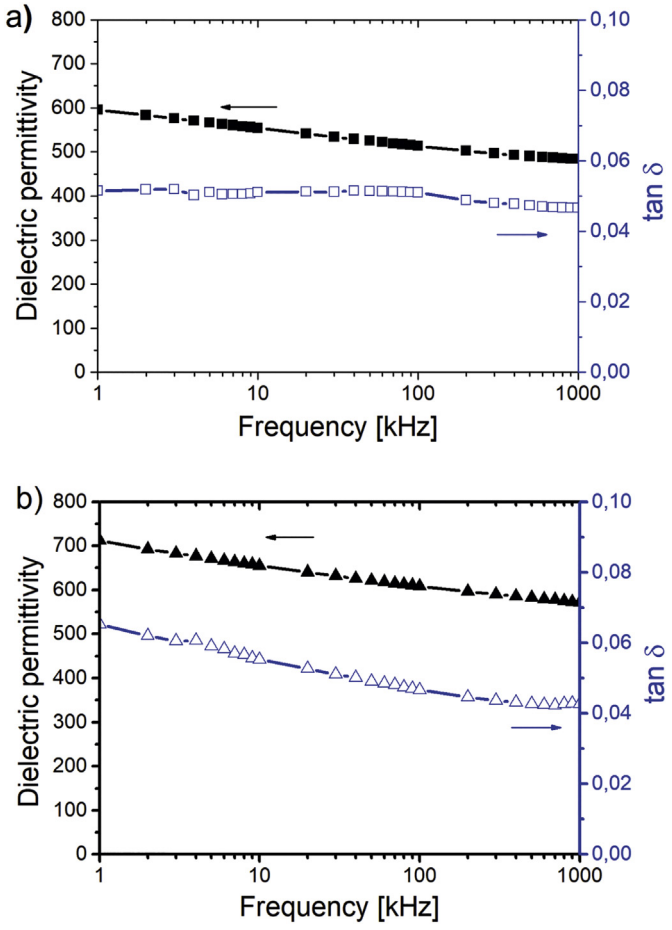

Fig. 9. Frequency dependence of dielectric permittivity and dielectric losses (tan δ) for a) P750 and b) P850.

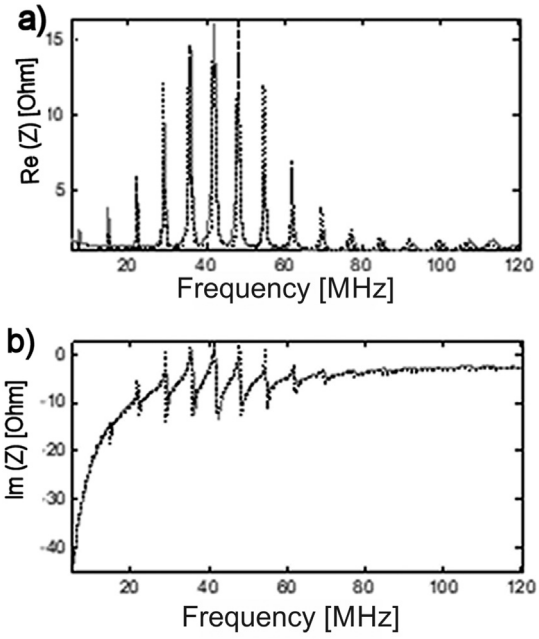

Fig. 10. Complex electrical impedance around the thickness-mode resonance of P850 (black dashed lines: experimental; grey solid lines: theoretical). a) Re (Z): real part; b) Im (Z): imaginary part.

Table 4
Properties of the three inert layers in the P850 thick film structure [32].

Inert layer	Material	t (μm)	ρ (kg/m^3)	Z (MRa)	α (dB/mm/MHz)
Substrate	Alumina	650	10,500	41	0.04
Top electrode	Gold	0.1	3240	62.6	–
Bottom electrode	Gold	6	3240	62.6	–

t: thickness, ρ: density, Z: acoustic impedance, α: attenuation coefficient.

Table 5
Properties of P850 and PN bulk.

Sample	ρ (%)	t (μm)	GS (μm)	$\varepsilon^S_{33}/\varepsilon_0$	c^D_{33} (GPa)	V_L (m/s)	e_{33} (C/m^2)	k_t (%)	δ_m (%)
P850	86 ± 3	15	1.2 ± 1	190	35	2280	3.5	46	5
PN bulk [34]	97 ± 2	500	5 ± 3	500	151	4400	12.5	48	1

ρ: relative density, t: thickness, GS: the mean grain size, $\varepsilon^S_{33}/\varepsilon_0$: dielectric constant at constant strain, c^D_{33}: elastic constant at constant electrical displacement, V_L: longitudinal wave velocity, e_{33}: piezoelectric coefficient, k_t: effective thickness-mode coupling factor, δ_m: mechanical losses.

3.5. Functional properties

The dielectric permittivity (ε) and dielectric losses (tan δ) as a function of frequency for the unpoled P750 and P850 are shown in Fig. 9 a and b, respectively. The ε decreased roughly linearly with the logarithm of the frequency, similar to the lead-zirconate-titanate thin films. This relationship is described in terms of Rayleigh's law, which illustrates the contribution of the irreversible displacement of the domain walls to the permittivity [28]. ε was larger for P850 than for P750 in the measured frequency range. Considering the identical chemical and phase compositions of the two samples, the difference in ε could be attributed mainly to the extrinsic contributions, such as grain size and density. For the PZT-based ceramic with an identical phase composition and density, it was shown that ε decreases as the grain size increases [29]. For the 850 °C sintered sample, the larger grain size contributes to the lower ε, while the larger density provides more dielectric phase in the thick film, which contributes to the larger ε. Altogether, they are responsible for the increase of ε. The tan δ ranges between 0.04 and 0.06. It is almost independent of frequency for P750 and decreases with increasing frequency for P850. In the latter case, the larger density and grain size could deliver a larger contribution of the domain structure to tan δ.

As expected, the dielectric properties of the thick films are lower than those of the PN bulk ceramic with an identical chemical composition, but a larger relative density of 96% and a grain size of 3.8 ± 1.6 μm, i.e., ε of 1500 and tan δ of 0.017 at 1 kHz [30]. The dielectric properties of these inkjet-derived thick films are comparable to the values reported for the PZTNb thick films prepared with other technologies and at higher temperatures of 950 °C: ε of 650–920 and tan δ of 0.056–0.12 at 1 kHz [24].

Only P850 was considered for a detailed electromechanical characterization. Due to the larger grain size and the higher relative density we expected higher associated electromechanical properties for this sample [31].

Fig. 10 shows the superimposition of the theoretical and experimental electrical impedance curves for P850 after the fitting process with the KLM scheme. The properties of the inert layers, i.e., the substrate, top and bottom electrode, used for the calculation are given in Table 4 [32]. The thickness of the bottom electrode was deduced from the SEM image (Fig. 8b). The coupling of the resonances in the alumina substrate and the piezoelectric thick film leads to multiple peaks [33]. The good agreement between the experimental and theoretical curves allowed us to deduced the electromechanical parameters for the piezoelectric thick film (Table 5). The electromechanical parameters for the bulk ceramic with identical nominal chemical composition sintered at 1250 °C are also given for comparison. The electromechanical characterization of the bulk was performed using the same procedure as for the thick films [34].

The comparison of the electromechanical properties of the thick film and the bulk with identical nominal chemical compositions revealed that the properties of P850 are lower than those of the bulk. This phenomenon can be attributed to many factors, including the fact that the P850 is constrained by the substrate, has a lower relative density and a smaller grain size than the bulk.

The lower $\varepsilon^S_{33}/\varepsilon_0$ for P850 is a result of two opposite contributions: the smaller grain size contributes to the larger $\varepsilon^S_{33}/\varepsilon_0$, while the lower density provides a smaller $\varepsilon^S_{33}/\varepsilon_0$. Based on the results, we presume that the density contribution prevails over that of the grain size.

The c^D_{33} of the P850 is significantly lower than that of the bulk. The value of c^D_{33} was deduced from a measurement of the longitudinal wave velocity V_L in piezoelectric materials using the following relationship [35]:

$$c_{33}{}^D = \rho \times V_L{}^2 \quad (1)$$

From Eq. (1) it is evident that the lower density and lower V_L of P850 contribute to the lower c^D_{33}.

The piezoelectric coefficient (e_{33}) is also lower for P850 than for the bulk. The lower e_{33} could be related to the more difficult domain orientation in fine grain sample due to pinning of the domain walls at the grain boundaries [29].

In contrast, the effective thickness coupling factor k_t is similar for the P850 and the bulk ceramic, i.e., 46% and 48%, respectively. The main reason is the trade-off between the piezoelectric, elastic and dielectric parameters in the k_t definition [35]:

$$k_t{}^2 = e_{33}{}^2/(c_{33}{}^D \times \varepsilon^S{}_{33}) \quad (2)$$

For P850 the values of e_{33}, c^D_{33} and ε^S_{33} were lower than those of the bulk but the relationship between these parameters results in a k_t, similar to that of the bulk. A similar value of k_t, i.e., 46%, was reported for thick films with a similar composition and thickness [3].

The mechanical losses (δ_m) are influenced by the porosity of the piezoelectric material and the frequency. They increase with the increase of these two parameters [36]. We measured the δ_m for P850 and for the bulk at the anti-resonance frequency. It was lower for the bulk (1.9 MHz) than for the P850 (76 MHz; resonance of the thick film in free mechanical conditions are considered). The higher anti-resonance frequency and larger porosity of P850 lead to a higher value of δ_m compared to the bulk

4. Conclusions

Piezoelectric thick films based on lead zirconate titanate are applicable in miniature electronic devices such as sensors, actuators, transformers, piezoelectric energy harvesters and transducers. Improvements in the device performances can be achieved through the use of piezoelectric material with desired chemical composition and microstructure, in particular density and grain size. In addition, the material should be patterned on the substrate in predefined geometry. Piezoelectric inkjet printing, a computer-controlled, low-cost and environmental-benign technology, is attractive technique for patterning thick-film structures. However, thick film is clamped on a rigid substrate and densifies in constrained conditions which frequently lead to the formation of defects. Here we report on the processing of thick films by the inkjet printing of an aqueous-based ink of $Pb(Zr_{0.53}Ti_{0.47})_{0.98}Nb_{0.02}O_3$ with 6 mol% of excess PbO and subsequent sintering. PbO enables sintering of thick film in the presence of the liquid phase as well as decrease the processing temperature to 850 °C.

An analysis of the ink revealed long-term stability of the nanosized particles in water, a viscosity of 10 mPas and a surface tension of 30

mN/m, which are suitable properties of the ink for selected commercial inkjet printer. The ink was jetted onto a gold-covered corundum substrate for an optimised waveform with a peak of 20 V and a duration of 8 ms. The spherical drops with a diameter of 50 μm jetted at a drop spacing of 20 μm formed a uniform, defect-free pattern with dimension of 4 mm × 4 mm. Based on the thermal analysis, we heated the structures at 400 °C, followed by sintering at 750 and 850 °C. Electron microscopy analysis of the sintered thick films revealed homogeneous, defect-free microstructures. The 850 °C-sintered film was 15 μm thick with a relative density of 86% and a grain size up to ~2 μm. The nano-sized powder and PbO contribute to the higher density of these thick films as compared to thick films prepared with other technologies but at 50 to 100 °C higher temperatures. The piezoelectric, elastic and dielectric properties of the thick film were lower than those of the bulk ceramic with an identical nominal chemical composition due to the lower relative density and the smaller grain size of the thick films. However, the effective thickness coupling factor k_t of the thick film was 46%, which is comparable to the k_t of the bulk. The results show that inkjet printing and subsequent sintering provide an effective way to process defect-free, homogeneous, single phase, thick films with a high thickness coupling factor.

Data availability

All data used during the study are available from the corresponding author by request.

Declaration of Competing Interest

The authors declare that they have no known competing financial interests or personal relationships that could have appeared to influence the work reported in this paper.

Acknowledgments

This work was supported by the Slovenian Research Agency (Grant P2-0105) and Bilateral project PROTEUS (Grant BI-FR-19-20-PROTEUS-08 and Grant 41658 ZM). Maja Majcen, Tina Bakarič, Kristijan Kovačič, Hugo Mercier, and Jena Cilenšek are acknowledged for their technical support.

References

[1] K. Uchino, The development of piezoelectric materials and the new perspective, in: K. Uchino (Ed.), Advanced Piezoelectric Materials Science and Technology, second ed.Woodhead Publishing, Duxford, Cambridge, Kidlington 2017, pp. 1–92, https://doi.org/10.1016/B978-0-08-102135-4.00001-1.

[2] M. Lee, C. Kim, W. Park, J. Cho, J. Paik, Y.H. Jeong, Energy harvesting performance of unimorph piezoelectric cantilever generator using interdigitated electrode lead zirconate titanate laminate, Energy 179 (2019) 373–382, https://doi.org/10.1016/j.energy.2019.04.215.

[3] D. Kuscer, J. Bustillo, T. Bakarič, S. Drnovšek, M. Lethicq, F. Levassort, Acoustic properties of porous lead zirconate titanate backing for ultrasonic transducers, IEEE Trans. Ultrason. Ferroelec. Freq. Control 67 (8) (2020) 1656–1666, https://doi.org/ 10.1109/TUFFC.2020.2983257.

[4] G. Estevesa, C.M. Fancher, M. Wallace, R. Johnson-Wilke, R.H.T. Wilke, S. Trolier-McKinstry, R.G. Polcawich, J.L. Jones, In situ X-ray diffraction of lead zirconate titanate piezoMEMS cantilever during actuation, Mater. Des. 111 (2016) 429–434, https://doi.org/10.1016/j.matdes.2016.09.011.

[5] A.E. Gurdal, S. Tuncdemir, K. Uchino, C.A. Randall, Low temperature co-fired multilayer piezoelectric transformers for high power applications, Mater. Des. 132 (2017) 512–517, https://doi.org/10.1016/j.matdes.2017.07.030.

[6] M. Kosec, D. Kuscer, J. Holc, Processing of ferroelectric ceramic thick films, in: L. Pardo, J. Ricote (Eds.), Multifunctional Polycrystalline Ferroelectric Materials, Springer, Dordrecht, Heidelberg, London, New York 2011, pp. 39–61, https://doi.org/10.1007/978-90-481-2875-4_2.

[7] D. Kuscer, Screen printing, Reference Module in Materials Science and Materials Engineering, Elsevier, 2020https://doi.org/10.1016/B978-0-12-803581-8.12082-X.

[8] H. Li, J. Liu, K. Li, Y. Liu, Piezoelectric micro-jet devices: A review, Sens. Actuator A Phys. 297 (2019), 111552, https://doi.org/10.1016/j.sna.2019.111552.

[9] D. Kuscer, J.Z. Shen, Advanced direct forming processes for the future, in: T. Kosmač, J.Z. Shen (Eds.), Advanced Ceramic for Dentistry, Elsevier, Waltham 2014, pp. 375–389.

[10] J.S. Gebauer, V. Mackert, S. Ognjanović, M. Winterer, Tailoring metal oxide nanopar-ticle dispersions for inkjet printing, J. Colloid Interface Sci. 526 (2018) 400–409, https://doi.org/10.1016/j.jcis.2018.05.006.

[11] J. Graff, R. Liang, M.Q. Le, J.-F. Capsal, F. Ganet, P.-J. Cottinet, Printable low-cost and flexible carbon nanotube buckypaper motion sensors, Mater. Des. 133 (2017) 47–53, https://doi.org/10.1016/j.matdes.2017.07.048.

[12] J. Yus, Z. Gonzalez, A.J. Sanchez-Herencia, A. Sangiorgi, N. Sangiorgi, D. Gardini, A. Sanson, C. Galassi, A. Caballero, J. Morales, B. Ferrari, Semiconductor water-based inks: miniaturized NiO pseudocapacitor electrodes by inkjet printing, J. Eur. Ceram. Soc. 39 (9) (2019) 2908–2914, https://doi.org/10.1016/j.jeurceramsoc. 2019.03.020.

[13] J. Lim, H. Jung, C. Baek, G.-T. Hwang, J. Ryu, D. Yoon, J. Yoo, K.-I. Park, J.H. Kim, All-inkjet-printed flexible piezoelectric generator made of solvent evaporation assisted $BaTiO_3$ hybrid material, Nano Energy 41 (2017) 337–343, https://doi.org/10.1016/j.nanoen.2017.09.046.

[14] I. Fraile, M. Gabilondo, N. Burgos, M. Azcona, F. Castro, Laser sintered ceramic coatings of PZT nanoparticles deposited by inkjet printing on metallic and ceramic substrates, Ceram. Int. 44 (2018) 15603–15610, https://doi.org/10.1016/j.ceramint.2018.05.225.

[15] O. Noshchenko, D. Kuscer, O.C. Mocioiu, M. Zaharescu, M. Bele, B. Malič, Effect of milling time and pH on the dispersibility of lead zirconate titanate in aqueous media for inkjet printing, J. Eur. Ceram. Soc. 34 (2) (2014) 297–305, https://doi. org/10.1016/j.jeurceramsoc.2013.08.002.

[16] T. Bakarič, B. Malič, D. Kuscer, Lead-zirconate-titanate-based thick-film structures prepared by piezoelectric inkjet printing of aqueous suspensions, J. Eur. Ceram. Soc. 36 (16) (2016) 4031–4037, https://doi.org/10.1016/j.jeurceramsoc.2016.06.038.

[17] D. Kuscer, O. Noshchenko, H. Uršič, B. Malič, Piezoelectric properties of ink-jet-printed lead zirconate titanate thick films confirmed by piezoresponse force micros-copy, J. Am. Ceram. Soc. 96 (9) (2013) 2714–2717, https://doi.org/10.1111/jace. 12532.

[18] Jettable Fluid Formulation Guidelines, https://www.fujifilm.com/us/en/business/inkjet-solutions/deposition-products/dmp-2850/support 2020 accessed 29.10.2020.

[19] R.K. Bordia, R. Raj, Sintering behaviour of ceramic films constrained by a rigid sub-strate, J. Am. Ceram. Soc. 68 (1985) 287–292, https://doi.org/10.1111/j.1151-2916.1985.tb15227.x.

[20] R.B. Atkin, R.M. Fulrath, Point defects and sintering of lead zirconate-titanate, J. Am. Ceram. Soc. 54 (5) (1971) 265–270 doi:10.1111/j.1151-2916.1971.tb12286.x.

[21] R. Krimholtz, D.A. Leeddom, G.L. Matthei, New equivalent circuit for elementary piezoelectric transducers, Electron. Lett. 6 (1970) 398–399, https://doi.org/10.1049/el:19700280.

[22] A.I. Kingon, J.B. Clark, Sintering of PZT ceramics: I. atmosphere control, J. Am. Ceram. Soc. 66 (4) (1983) 253–256 doi:10.1111/j.1151-2916.1983.tb15708.x.

[23] A.I. Kingon, J.B. Clark, Sintering of PZT ceramics: II. Effect of PbO content on densification kinetics, J. Am. Ceram. Soc. 6 (4) (1983) 256–260. doi:10.1111/j.1151-2916.1983.tb15709.x.

[24] M.S. Bernardo, B. Malič, D. Kuscer, PZT-based thick films prepared by electrophoretic deposition from suspensions with different alcohol-based solvents, J. Electrochem. Soc. 162 (11) (2015) D3040–D3048, https://doi.org/10.1149/2.0151511jes.

[25] G.S. Snow, Fabrication of transparent electrooptic PLZT ceramic by atmosphere Sintering, J. Am. Ceram. Soc. 56 (2) (1973) 91–96 doi:10.1111/j.1151-2916.1973.tb12365.x.

[26] R.K. Bordia, S.-J.L. Kang, E.A. Olevsky, Current understanding and future research directions at the onset of the next century of sintering science and technology, J. Am. Ceram. Soc. 100 (2017) 2314–2352, https://doi.org/10.1111/jace.14919.

[27] K.H. Hardt, H. Rau, PbO vapour pressure in the $Pb(Ti_{1-x}Zr_x)O_3$ system, Solid State Commun. 7 (1969) 41–45, https://doi.org/10.1016/0038-1098(69)90688-7.

[28] D.V. Taylor, D. Damjanovic, Evidence of domain wall contribution to the dielectric permittivity in PZT thin films at sub-switching fields, J. Appl. Phys. 82 (4) (1997) 1973–1975, https://doi.org/10.1063/1.366006.

[29] C.A. Randall, N. Kim, J.-P. Kucera, W. Cao, T.R. Shrout, Intrinsic and extrinsic size effects in fine-grained morphotropic-phase-boundary lead zirconate titanate ce-ramics, J. Am. Ceram. Soc. 81 (3) (1998) 677–688 doi:10.1111/j.1151-2916.1998. tb02389.x.

[30] D. Kuscer, T. Rojac, D. Belavič, M.S. Zarnik, A. Bradeško, T. Kos, B. Malič, M. Boerrigter, D.M. Martin, M. Faccini, Integrated piezoelectric vibration system for fouling mitiga-tion in ceramic filtration membranes, J. Membr. Sci. 540 (2017) 277–284, https://doi.org/10.1016/j.memsci.2017.06.054.

[31] W. Cao, C.A. Randall, Grain size and domain size relations in bulk ceramic ferroelec-tric materials, J. Phys. Chem. Solids 57 (10) (1996) 1499–1505, https://doi.org/10.1016/0022-3697(96)00019-4.

[32] B. Mueller, Additive manufacturing technologies–Rapid prototyping to direct digital manufacturing. Assembly Automation, (2012).

[33] M. Lukacs, T. Olding, M. Sayer, R. Tasker, S. Sherrit, Thickness mode material con-stants of a supported piezoelectric film, J. Appl. Phys. 85 (5) (1999) 2835–2843, https://doi.org/10.1063/1.369603.

[34] A.-P. Abellard, Patterned Piezoelectric Thick Films by Electrophoretic Deposition for High-Frequency Ultrasound Transducers, Doctoral Thesis, Jožef Stefan International Postgraduate School, Ljubljana, 2016https://doi.org/10.13140/RG.2.1.2024.6247.

[35] T. Ikeda, Fundamentals of Piezoelectricity, Oxford University Press, New York, 1990.

[36] E.I. Petrova, M.A. Lugovaya, I.A. Shvetsov, N.A. Shvetsova, A.N. Reznichenko, A.N. Rybyanets, Porous and composite materials based on lead-free ferroelectric ceramics for ultrasonic transducers applications, in: I.A. Parinov, S. Chang, V.K. Gupta (Eds.), Advanced Materials: Proceedings of the International Conference on Physics and Mechanics of New Materials and their Applications, Springer, Cham 2018, pp. 49–63.